Practical post-Kohn–Sham methods for time-reversal symmetry breaking references

Christof Holzer*

Institute of Theoretical Solid State Physics, Karlsruhe Institute of Technology (KIT), Wolfgang-Gaede-Straße 1, 76131 Karlsruhe, Germany

E-mail: christof.holzer@kit.edu

February 7, 2023

Abstract

Reduced scaling algorithms based on auxiliary subspace methods for correlation energies from the random phase approximation (RPA) as well as correlation self-energies from the *GW* method are derived for time-reversal symmetry breaking Kohn–Sham (KS) references. This allows for an efficient evaluation of RPA energies and *GW* quasiparticle energies for molecular systems with KS references that break time-reversal symmetry. The latter occur for example in magnetic fields. Furthermore, KS references for relativistic open-shell molecules also break time-reversal symmetry due to the single determinant ansatz used. Errors of the newly developed reduced-scaling algorithms are shown to be negligible compared to reference implementations, while the overall computational scaling is reduced by two orders of magnitude. Ionization energies obtained from the *GW* approximation are shown to be robust even for the electronically complicated group of trivalent lanthanoid ions. Starting from *GW* quasiparticle energies, it is subsequently shown that light-matter interactions of these systems can be calculated using the Bethe–Salpeter equation (BSE). Using the combined *GW*-BSE method, the absorption and emission spectra of a molecular europium(III) complex can be obtained including spin-orbit coupling.

1 Introduction

The random phase approximation (RPA)[1–6] and its Greens function based sibling, the *GW* method,[7–9] have well advanced in molecular quantum chemistry in the past few years. Initial molecular implementations of these post-Kohn–Sham (KS) methods focused on field-free, non-relativistic molecular systems. Extensions of the RPA[10] and the *GW* method[11,12] to time-reversal symmetry (TRS) breaking systems have also been achieved. Starting from a steep N^6 scaling,[13] algorithms to bring down the scaling to $N^3 - N^4$ have since been developed.[14,15] These improved algorithms for molecular systems replaced the initial spectral representation of the plasmon formula[6,16] by an integration over the imaginary axis using an auxiliary subspace. Similar numerical integration techniques have further been devised for molecular implementations of the *GW* method, lowering the initial N^6 effort[9] to $N^3 - N^4$.[17–21] However, auxiliary subspace based variants of the RPA and the *GW* method could only be derived for KS references that obey time-reversal symmetry.[19,22] Contrary, Hartree–Fock (HF) and Kohn–Sham references that break TRS resisted these reformulations, locking them to the steep N^6 scaling of the plasmon formula. Even worse, the complex algebra introduced by the two- or four-component spinor formulation of the underlying KS density functional theory (DFT) methodology introduces a sizable prefactor, ranging from 256-2048 depending on the exact task.[12,19,22,23] This severely limits the applicability of the RPA and the *GW* method to TRS breaking KS references, restricting them to molecular systems with less than a handful of non-hydrogen atoms. This has two major implications for actual calculations. First, this is a major drawback for relativistic open-shell systems, as time-reversal symmetry may be (artificially) broken for those in variational single-determinant approaches like HF or KS-DFT.[24,25] Second, within magnetic fields time-reversal symmetry need not be obeyed, further limiting the range of molecular systems accessible by the RPA and the *GW* method.[24,25]

This paper aims to alleviate this drawback, providing the derivations and formulas needed to calculate RPA correlation energies as well as *GW* self-correlation energies for TRS breaking systems using canonical auxiliary subspace based N^4 scaling algorithms. These new RPA and *GW* algorithms allow for assessing molecular systems with up to a few thousand basis functions. Furthermore, the derived canonical RPA and *GW* algorithms provide entry points for even lower scaling algorithms.[26–31] To outline the capabilities of the newly developed algorithms, molecular systems in magnetic fields are investigated. The RPA can for example be used for a robust description of the energy change of molecular system as a function of the applied magnetic field. This is used to study a metal-organic Mn(III) complex, which was among the first to be shown to a undergo spin state transition in a magnetic fields accessible in current laboratories.[32,33] Furthermore, light-matter interactions of the trivalent lanthanoids are investigated as prime examples for open-shell relativistic systems. Complexes and materials containing trivalent lanthanoids, Ln(III), are at the heart of several modern applications of photonic materials and molecular systems.[34] A unique property of trivalent lanthanoids is that they basically maintain their atomic-like spectra even when incorporated into a molecular system.[35] The corresponding Ln^{3+} ions are known to be troublesome for many quantum chemical methods, including time-dependent density functional theory, CASSCF, and even coupled-cluster based methods. Meaningful studies of them have only been possible using relativistic configuration interaction methods. The latter have been able to provide accurate results, but at tremendous costs.[36,37] Furthermore, complexes including trivalent lanthanoids are prime examples of diverse light-matter interactions in open-shell relativistic systems. Neglecting spin-orbit coupling (SOC) immediately leads to large deviations, given that without SOC the splitting of the atomic-like $4f$ shell is completely neglected. As the quasiparticle energies obtained from the *GW* method provide suitable starting points for the static-screened Bethe–Salpeter equation (BSE) method,[38–42] light-matter interaction of TRS breaking systems can also be asssed based on the new developments outlined

in this work. As example, a model system being based on a real Eu^{3+} molecular assembly showing strong circular polarized light emission is investigated using the adapted TRS breaking version of the *GW*-BSE method. It can be shown that sufficiently accurate predictions can be made using this new method, even for electronically complex systems.

2 Theory

This work is concerned with the post-KS RPA correlation energies and *GW* self-correlation energies for general time-reversal symmetry breaking KS references. Such KS references for example occur in magnetic fields, or during the variational KS treatment of relativistic systems with unpaired electrons. The latter is due to the single-determinant nature of the KS-DFT ansatz.[25] In both cases, the KS equations take at least a two-component (2c) form, as demanded by the Pauli spin matrices. The corresponding complex two-component molecular spinors obtained from the KS equation are expanded in terms of atomic basis functions as

$$q = \phi_q(x) = \sum_{\mu} \left\{ c_{\mu\alpha,q}\chi(r)\alpha(\sigma) + c_{\mu\beta,q}\chi(r)\beta(\sigma) \right\}. \quad (1)$$

$x = \{r,\sigma\}$, $\alpha(\sigma)$ and $\beta(\sigma)$ are spin functions, while $c_{\mu\alpha,q}$ and $c_{\mu\beta,q}$ denote the complex expansion coefficients obtained from the converged 2c KS equations. Furthermore, in the following sections the indices $i,j,k,\ldots$ $(a,b,c,\ldots)$ denote occupied (virtual) spinors, $p,q,r\ldots$ denote general spinors, and upper case indices $P,Q,R,\ldots$ will denote auxiliary basis functions. The exact kind of the atomic orbital (AO) functions χ is only of technical importance. They can be real, as e.g. Gaussian-type atomic orbitals (GTOs) or numerical atomic orbitals. Alternatively, they can be complex, as e.g. London atomic orbitals (LAOs). In this work, real GTOs and complex LAOs will be used as AOs. Note that the resulting spinors are always complex. Contrary, the auxiliary basis functions can always be chosen to be real, even in the case of complex AO basis functions.[43] For the general structure of the HF and KS-DFT Hamiltonian including the implications of time-reversal symmetry, the reader is referred to Ref. 25.

2.1 Correlation energies for time-reversal symmetric references from the random phase approximation

A rather general way to obtain correlation energies in the random phase approximation is the "plasmon formula",[4]

$$E^{\mathrm{C,RPA}} = \frac{1}{2} tr(\Omega^{+} - \mathbf{A}) \quad (2)$$

where Ω^{+} is a diagonal matrix collecting all positive RPA excitation energies. The latter can be obtained from the eigenvalue problem

$$\begin{pmatrix} \mathbf{A} & \mathbf{B} \\ -\mathbf{B} & -\mathbf{A} \end{pmatrix} \begin{pmatrix} \mathbf{X} & \mathbf{Y}^{*} \\ \mathbf{Y} & \mathbf{X}^{*} \end{pmatrix} = \begin{pmatrix} \mathbf{X} & \mathbf{Y}^{*} \\ \mathbf{Y} & \mathbf{X}^{*} \end{pmatrix} \begin{pmatrix} \Omega^{+} & \mathbf{0} \\ \mathbf{0} & -\Omega^{+} \end{pmatrix} \quad (3)$$

where $\mathbf{X}$ and $\mathbf{Y}$ satisfy the condition $\mathbf{X}\mathbf{X}^{\dagger} - \mathbf{Y}\mathbf{Y}^{\dagger} = \mathbf{1}$. The orbital rotation matrices $\mathbf{A}$ and $\mathbf{B}$ are given as

$$A_{ia,jb} = (\varepsilon_a - \varepsilon_i)\delta_{ab}\delta_{ij} + v_{ia,bj} \quad (4)$$

$$B_{ia,jb} = v_{ia,jb}, \quad (5)$$

where ε_p refers to the KS orbital energies, and $v_{pq,rs} = (pq|sr)$ is the bare Coulomb integral. While Eq. 2 is generally applicable, its steep N^6 scaling with increasing system size is the clear downside, quickly rendering the RPA unfeasible for many systems. This type of solution will be referred to as spectral solution in the following.

Eshuis *et al.* have shown that, for non-relativistic KS references, Eq. 2 can be rewritten as[14]

$$E^{\mathrm{C,RPA}} = \frac{1}{2} tr(\mathbf{M}^{1/2} - \mathbf{A}) \quad (6)$$

with the matrix $\mathbf{M}$ being defined as

$$\mathbf{M} = (\mathbf{A}-\mathbf{B})^{1/2}(\mathbf{A}+\mathbf{B})(\mathbf{A}-\mathbf{B})^{1/2}, \quad (7)$$

exploiting the diagonal structure of $(\mathbf{A}-\mathbf{B})$. Subsequently applying the resolution-of-the-identity (RI) approximation,[14]

$$v_{pq,rs} \approx \sum_{P} R_{P,rs} R^{*}_{P,rs} \quad (8)$$

$$R_{P,rs} = \sum_{Q} [V^{-1/2}]_{PQ}(Q|rs) \quad (9)$$

$$V_{PQ} = (P|Q), \quad (10)$$

and expressing $\mathbf{M}^{1/2}$ as an integral

$$tr(\mathbf{M}^{1/2}) = 2\int_{-\infty}^{\infty} \frac{d\omega}{2\pi} tr\left[\mathbf{1} - \omega^2 \left(\mathbf{M} + \omega^2 \mathbf{1} \right)^{-1} \right], \quad (11)$$

a fast yet accurate path to calculate RPA correlation energies is obtained. The final equation valid for non-relativistic KS references reads[14]

$$E^{\mathrm{C,RIRPA}} = \int_{-\infty}^{\infty} \frac{d\omega}{4\pi} tr\left[ln(\mathbf{1}_{PQ} + \widetilde{\Pi}_{PQ}(\omega)) - \widetilde{\Pi}_{PQ}(\omega)) \right], \quad (12)$$

where $\widetilde{\Pi}$ is defined as

$$\widetilde{\Pi}_{PQ}(\omega) = 2Re \sum_{kc} \left[\frac{(\varepsilon_k - \varepsilon_c) R_{p,kc} R^{*}_{Q,kc}}{(\varepsilon_k - \varepsilon_c)^2 + \omega^2} \right]. \quad (13)$$

Eq. 12 reduces the scaling to N^4, being two orders of magnitude faster than the spectral solution of Eq. 2. Kühn was able to extend this ansatz to field-free, closed-shell TRS two- and four-component (4c) references.[22]

2.2 Correlation energies for time-reversal symmetry breaking references from the random phase approximation

For general complex 2c or 4c KS references $(\mathbf{A}-\mathbf{B})$ is no longer diagonal, but complex and non-symmetric. $(\mathbf{A}+\mathbf{B})$ is also no longer hermitian, but again complex and non-symmetric. As a consequence, Eq. 3 cannot be simplified to a standard hermitian eigenvalue problem with halved dimensions. This key step in the derivation of Refs. 14 and 22 is therefore no longer valid for general 2c or 4c KS references. A simple solution is obtained by rewriting the initial Langreth-Perdew expression.[44] The latter defined the correlation energy in the random phase approximation as

$$E^{\mathrm{C,RPA}} = \int_{-\infty}^{\infty} \frac{d\omega}{4\pi} tr[ln(\mathbf{1} + \chi_0(i\omega)\mathbf{v}) - \chi_0(i\omega)\mathbf{v})]. \quad (14)$$

where $\chi_0(\omega)$ refers to the non-interacting KS response function

$$\chi_0(\omega)_{kc,kc} = (\varepsilon_k - \varepsilon_c + \omega)^{-1} \quad (15)$$

$$\chi_0(\omega)_{ck,ck} = (\varepsilon_k - \varepsilon_c - \omega)^{-1}. \quad (16)$$

In the next step, the Coulomb matrix $\mathbf{v}$ is decomposed as,

$$\varepsilon_{pq,rs}(\omega) = \chi_0(\omega)_{pq,tu} v_{tu,rs} \approx \chi_0(\omega)_{pq,tu} R_{P,tu} R^*_{Q,rs}, \tag{17}$$

helping in exploiting its rank deficiency. Analysis of the matrices in Eq. 17 reveals that the dielectric function $\varepsilon(\omega)$ can be assumed to be sufficiently well behaved for the cases occurring in the calculation of RPA correlation energies and *GW* self-correlation energies. The real part of the non-interacting KS response function $\chi_0(\omega)$ is positive definite if the KS reference has a non-vanishing gap. Therefore, for every purely imaginary value $i\omega$, $\chi_0(i\omega)$ is located in the first and fourth quadrant of the complex plane with $\chi_0(i\omega) = \chi_0(-i\omega)^*$, with mirror symmetry w.r.t. the real axis. The determinant of $\chi_0(i\omega)$ is therefore real for any purely imaginary frequency $i\omega$. Furthermore, the determinant is real for any purely real frequency ω. Additionally, the Coulomb matrix $\mathbf{v}$ is hermitian and positive semi-definite. A decomposition of the latter is therefore always possible. If available, the RI approximation is the natural choice for this decomposition. A pivoted Cholesky decomposition of the Coulomb matrix would otherwise be possible, too. Inserting Eq. 17 into Eq. 14, using the cyclic invariance of the trace, and the relation $tr(ln(\Pi)) = ln(det(\Pi))$, the RPA energy can be rewritten as

$$E^{\text{C,2c-RIRPA}} = \int_{-\infty}^{\infty} \frac{d\omega}{4\pi} \left(\left\{ ln(det\left[\mathbf{1} + \Pi_{PQ}(i\omega)\right] \right\} - tr\left[\Pi_{PQ}(i\omega)\right] \right). \tag{18}$$

$\Pi_{PQ}(\omega)$ in Eq. 18 denotes the general complex interaction kernel, emerging from the dielectric function in the auxiliary subspace representation. The latter is given by

$$\Pi_{PQ}(\omega) = \sum_{kc} \left[\frac{R_{P,kc} R^*_{Q,kc}}{\varepsilon_k - \varepsilon_c + \omega} + \frac{R_{P,ck} R^*_{Q,ck}}{\varepsilon_k - \varepsilon_c - \omega} \right]. \tag{19}$$

For purely imaginary values of $i\omega$, $\Pi(i\omega)$ is real and non-symmetric, possibly yielding complex eigenvalues. Direct matrix logarithms as used in Eqs. 12 and 14 are therefore problematic, but are avoided in Eq. 18. As the determinant follows the relation $det(\boldsymbol{\chi_0}\Pi) = det(\boldsymbol{\chi_0}) det(\Pi)$, it follows that $det(\Pi) \in \mathbb{R}^+$ if $R_{P,pq}$ has no linearly dependent columns. The latter condition is fulfilled if the chosen set of auxiliary basis functions $|P)$, or columns of the pivoted Cholesky decomposition, are linearly independent. The invertibility of the first term in Eq. 18, $[\mathbf{1} + \Pi(i\omega)]$, can then be proven through the Woodbury matrix identity,[45] as the unit matrix is trivially invertible. A suitable decomposition of $\Pi(i\omega)$ also exists, simply guaranteed by its real, positive, non-zero determinant. The determinant and inverse of the real, non-symmetric matrix $[\mathbf{1} + \Pi(i\omega)]$ can therefore safely be evaluated. In this work, they are obtained from a pivoted LU decomposition. The real determinant also hints that complex eigenvalues of $[\mathbf{1} + \Pi(i\omega)]$ occur in complex conjugate pairs. Using the symmetry properties of Π,[19]

$$\Pi(i\omega) = \Pi^{\dagger}(-i\omega) = \Pi^{T}(-i\omega) = \Pi^{*}(i\omega), \tag{20}$$

Eq. 18 can be further simplified. As the trace and determinant of Π are invariant to transpositions, the integral in Eq. 18 only needs to be carried out in the interval $[0;\infty]$. The final expression is therefore reduced to

$$E^{\text{C,2c-RIRPA}} = \int_{0}^{\infty} \frac{d\omega}{2\pi} \left(\left\{ ln(det\left[\mathbf{1} + \Pi(i\omega)\right] \right\} - tr\left[\Pi(i\omega)\right] \right). \tag{21}$$

Eq. 21 is numerically well behaved, and allows for the computation of direct RPA energies for arbitrary KS references with N^4 scaling.

2.3 Correlation self-energies for time-reversal symmetry breaking references from the GW approximation

Similar to the random phase approximation, *GW* correlation self-energies for TRS breaking systems are tedious to compute using the spectral solution, needing to solve Eq. 3.[9,11] This severely limits the range of accessible molecular systems for *GW* to those consisting of only a handful of atoms. Similar to the previous Sec. 2.2, this can drawback can however be alleviated. The *GW* self-energy $\Sigma(x,x',\omega)$

$$\Sigma(x,x',\omega) = \int_{-\infty}^{\infty} W(x,x',\omega') G(x,x',\omega+\omega') d\omega' \tag{22}$$

is calculated from the Green's function

$$G(x,x',\omega) = \sum_q \frac{\phi_q(x)\phi_q^*(x')}{\omega - \varepsilon_q^{\text{F}} + i\delta sgn(\varepsilon_q^{\text{F}})} \tag{23}$$

and the screened exchange

$$W(x,x',\omega) = \int \varepsilon^{-1}(x,x'',\omega) v(r''-r') dx'', \tag{24}$$

where $\varepsilon_q^{\text{F}} = \varepsilon_q - \varepsilon^{\text{F}}$ is the difference between the energy of q-th spinor and the Fermi level. The dielectric function ε is implicitly defined by Eq. 17. Using contour deformation (CD), and subtracting the exchange part from Eq. 22, the remaining correlation self-energy Σ_q^{C} can be split into two parts[19,46]

$$\Sigma_q^{\text{C}}(\omega^{\text{F}}) = R_q^{\text{C}}(\omega^{\text{F}}) + I_q^{\text{C}}(\omega^{\text{F}}). \tag{25}$$

In Eq. 25, $\omega^{\text{F}} = \omega - \varepsilon^{\text{F}}$ is the frequency shift w.r.t. the Fermi level. Proceeding similar to Ref. 19 then yields updated formulas for the correlation self-energy of the q-th spinor in for TRS breaking KS reference

$$I_q^{\text{C}}(\omega) = \frac{1}{4\pi} \sum_p \int_{-\infty}^{\infty} \frac{1}{\omega^{\text{F}} - \varepsilon_p^{\text{F}} + \omega'} \left\{ W_{pq,pq}(i\omega') - v_{pq,pq} \right\} d\omega' \tag{26}$$

$$R_q^{\text{C}}(\omega) = \sum_p f_p \left\{ W_{pq,pq}(\omega^{\text{F}} - \varepsilon_p^{\text{F}}) - v_{pq,pq} \right\}. \tag{27}$$

f_p in Eq. 27 is the contribution of the residue,

$$f_p = \begin{cases} +1 \text{ if } \omega^{\text{F}} > \varepsilon_p^{\text{F}} > 0 \\ -1 \text{ if } \omega^{\text{F}} < \varepsilon_p^{\text{F}} < 0 \\ +\frac{1}{2} \text{ if } \omega^{\text{F}} = \varepsilon_p^{\text{F}} > 0 \\ -\frac{1}{2} \text{ if } \omega^{\text{F}} = \varepsilon_p^{\text{F}} < 0 \\ 0 \text{ else,} \end{cases} \tag{28}$$

where the cases $\{1,-1\}$ refer to poles inside the contour, $\{\frac{1}{2},-\frac{1}{2}\}$ to cases with the poles on the contour, and $f_p = 0$ to poles outside the contour. Inserting Eqs. 17 and 24 into Eqs. 26 and 27 yields the final expressions needed to calculate the correlation self-energy. The key point is the construction of the screened exchange W,

$$W_{pq,rs}(\omega) = \sum_{PQ} R^*_{P,pq} [\Pi_{PQ}(\omega)]^{-1} R_{Q,rs} \tag{29}$$

which is possible for every real or imaginary frequency ω as outlined in the previous section. In passing, it is noted that the number of evaluations of Eq. 19 needed to construct Eq. 26 can be halved by exploiting the symmetry constraints of Eq. 20. However, unlike for field-free non-relativistic or the RPA energy, the integral bounds of

Eq. 26 cannot be halved. This is a consequence of TRS breaking, as $\mathbf{W}(i\omega) \neq \mathbf{W}(-i\omega)^\dagger$. From the obtained correlation self-energies, the q-th *GW* quasiparticle energies can be calculated as usual as[9]

$$\varepsilon_q^{\mathrm{QP}}(\omega) = \varepsilon_q + Z\left\langle \phi_q \middle| \Sigma^{\mathrm{X}} + \Sigma^{\mathrm{C}}(\omega) - V^{\mathrm{KS}} \middle| \phi_q \right\rangle, \tag{30}$$

where Z in Eq. 30 is a linearization factor used in non-iterative G_0W_0. Z is set to 1 for iterative solution of the *GW* quasiparticle equations.[9] Using Eq. 30, it is now straightforward to calculate quasiparticle corrections for TRS breaking KS references in the G_0W_0 and ev*GW* approximation.

2.4 Charge-neutral excited states from the Bethe–Salpeter equation

While the RPA and *GW* method yield ground-state correlation energies, excited states and light-matter interaction in general can subsequently be accessed using many-body perturbation theory by the means of the static-screened Bethe–Salpeter equation (BSE). From a set of *GW* quasiparticle energies and the corresponding 2c spinors, the *GW*-BSE method allows for the calculation of charge-neutral excited states. In matrix form, the static-screened BSE adopts the same structure as Eq. 3, with the matrices **A** and **B** being replaced by

$$A_{ia,jb} = (\varepsilon_a - \varepsilon_i)\delta_{ab}\delta_{ij} + v_{ia,bj} + W_{ab,ij}(\omega = 0) \tag{31}$$

$$B_{ia,jb} = v_{ia,jb} + W_{ja,ib}(\omega = 0), \tag{32}$$

where $W_{pq,rs}(\omega = 0)$ is the screened exchange outlined in Eq. 24 at a frequency of zero. As outlined in Ref. 19, no special care needs to be taken for $W_{pq,rs}(\omega = 0)$ even if time-reversal symmetry is broken, as $\Pi_{PQ}(\omega = 0)$ is always real and symmetric. Therefore, the 2c linear response BSE[19] and the corresponding 2c damped response BSE formalism[47] are directly applicable. For a more detailed discussion of the 2c BSE, the reader is therefore referred to Refs. 19 and 47. In principle, the TRS breaking *GW*-BSE ansatz can also be used for property calculations in general, as it has been outlined for the non-relativistic case.[48] Here, it shall be stressed that Eq. 3 will yield excitations and de-excitations due its structure. In case of an excited state KS reference, de-excitations will therefore mix with excitations. To distinguish excitations from de-excitations in the positive branch of Eq. 3, the norm

$$|XX^\dagger - YY^\dagger| \begin{cases} > 0 \text{ if excitation} \\ < 0 \text{ if de-excitation} \end{cases} \tag{33}$$

can be used. Depending on the sign of the norm, the resulting vector $\{X, Y\}$ is then normalized to 1 or -1 using Eq. 33.

3 Computational details

RI-RPA correlation energies as outlined in Eq. 21 and correlation self-energies required for RI-G_0W_0 and RI-evGW[49] as outlined in Eq. 25 have been implemented for general KS references in a development version of TURBOMOLE V7.7.[50] The corresponding subroutines have been parallelized using OpenMP, also being capable of offloading to graphics processing units (GPUs). The Bethe–Salpeter equation part implemented in TURBOMOLE was enhanced to be able to distinguish between excitations and de-excitations using the norm as outlined in Sec. 2.4. Furthermore, 2c natural transition orbitals (NTOs) for the BSE were implemented as suggested by Ref. 51.

In the following sections, the density functionals PBE,[52] PBE0,[53] TPSSh,[54] ωB97M,[55] and the recently developed local hybrid density functional TMHF[56] were used. Hybrid, range-separated, and local hybrid functionals have shown to perform well for determining quasiparticle energies from the *GW* approximation and excited states from the the *GW*-BSE method.[57–59] KS reference states were converged to at least 10^{-8} E_h and 10^{-7} E_h for differences in energies and the difference density, respectively. Tight integration grids were used (gridsize 4 for DFT,[60] for standard and hybrid DFT functionals, gridsize ultrafine[61] for the TMHF local hybrid). For TPSSh, ωB97-M, and TMHF, a current-dependent ansatz was used.[62] Current-density dependent Kohn–Sham references have shown to be important for open-shell systems,,[62,63] especially when spin-orbit coupling is present. The geometries of the [Mn(pyrol)$_3$(tren)] complex, labelled as [Mn(taa)], with two and four unpaired electrons were optimized using the r^{2}SCAN[64] density functional in conjunction with the def2-TZVPP basis set.[65] The geometry of the [Eu(PDCA)$_3$]$^{3+}$ complex was taken and adapted from Ref. 66, and hydrogen positions were re-optimized using the r^{2}SCAN density functional in conjunction with x2c-QZVPPall-2c (Eu) and x2c-TZVPPall-2c (others) basis set.[67,68] For [Eu(PDCA)$_3$]$^{3+}$, the local X2C Hamiltonian was used, in conjunction with a finite nucleus model.[68,69] All optimized geometries can be found in the supporting information of this paper. All DFT calculations made use of the RI approximation for the Coulomb part using the corresponding auxiliary basis sets fitted to ground state energies.[67,70] The RI approximation was used in all RPA and *GW* calculations. For lanthanoids, the same uncontracted auxiliary basis sets as for the ground state were used.[67] For all remaining elements, the specialized auxiliary basis sets fitted to MP2 energies were used.[71] Calculations in magnetic fields are performed using gauge-invariant London atomic orbitals.

4 Results and discussion

4.1 Analysis for a two-electron system in an external magnetic field

For a two-electron system like the Helium atom, it is straightforward to precisely calculate all integrals outlined in section 2. Results at magnetic field strengths of 0.0, 0.1, 0.25, and 0.5 a.u. (1 a.u. = 235.051 tesla) for a PBE/aug-cc-pV5Z KS reference are given in Tab. 1.

In the field-free case, evaluating Eq. 26 leads to the same results for both electrons. Eq. 27 yields two contours for both electrons, $(\omega_p^{\mathrm{F}} - \varepsilon_p^{\mathrm{F}})$ and $(\omega_p^{\mathrm{F}} - \varepsilon_q^{\mathrm{F}})$, with f_p tending to $\pm\frac{1}{2}$ for both $\omega_p^{\mathrm{F}} = \omega_q^{\mathrm{F}}$ and $\varepsilon_p^{\mathrm{F}} = \varepsilon_q^{\mathrm{F}}$. However, the contour of ω_p^{F} vanishes for $\varepsilon_q^{\mathrm{F}}$ due to the symmetry relation $\phi_q = \phi_p^*$, which is valid in the time-reversal symmetric case. Note that only the contour of the orbital itself contributes to the residue R_q^{C}, but not its time-reversal (Kramers[72]) partner. If a finite magnetic field is turned on, but the system is not yet spin-polarized, this behavior is partly retained. The correlation self-energy obtained for both electrons is equivalent. The quasiparticle energies $\varepsilon^{\mathrm{QP}}$ are simply split by the spin s effect, as are the Kohn–Sham spinor energies. This could mislead one to the conclusion that a TRS breaking ansatz is not explicitly needed in a spin-unpolarized case. While the latter assumption is indeed true for the residues R_q^{C}, which are obtained from the hermitian quantity $\Pi(\omega)$, it does not hold for the integral I_q^{C}. The latter is real but already non-symmetric. The non-symmetric parts originate from the loss of time-reversal symmetry between the former Kramers partners, which are no longer related in a magnetic field even in a spin-unpolarized KS reference. This asymmetry is ultimately also the reason why the RI-RPA ansatz of Kühn[22] fails for TRS breaking KS references even in spin-unpolarized cases. When the system is fully spin-polarized, the loss of time-reversal symmetry becomes

Table 1: Quasiparticle energies ($\varepsilon^{\mathrm{QP}}$), Kohn–Sham spinor energies ($\varepsilon^{\mathrm{KS}}$), Kohn–Sham potential ($v^{\mathrm{KS}}$), exchange self-energy (Σ^{X}), and the imaginary ($I^{\mathrm{C}}_{p/q}$) and real ($R^{\mathrm{C}}_{p/q}$) contours contributing to the correlation self-energy of the spin-up and spin-down electron of a Helium atom in a magnetic field ranging from 0 to 0.5 atomic units (1 a.u. = 235.051 tesla). Calculations performed using a 2c PBE/aug-cc-pV5Z KS reference. All values in eV.

	$\varepsilon^{\mathrm{QP}}$	$\varepsilon^{\mathrm{KS}}$	v^{KS}	Σ^{X}	$I^{\mathrm{C}}_{p/q}$	$R^{\mathrm{C}}_{p/q}(0)$	$R^{\mathrm{C}}_{p/q}(\Delta\varepsilon_{p/q})$	$\Sigma^{\mathrm{C}}_{p/q}$
B = 0.00 a.u., S = 0, $E^{\mathrm{C,RPA}}$=-0.08260730								
ε_p	−24.446	−15.763	−18.211	−27.575	−2.098	2.779	0.000	0.680
ε_q	−24.446	−15.763	−18.211	−27.575	−2.098	2.779	0.000	0.680
B = 0.10 a.u., S = 0, $E^{\mathrm{C,RPA}}$=-0.08257630								
ε_p	−25.778	−17.067	−18.230	−27.607	−2.098	2.764	0.000	0.666
ε_q	−23.056	−14.346	−18.230	−27.607	−2.098	2.764	0.000	0.666
B = 0.25 a.u., S = 0, $E^{\mathrm{C,RPA}}$=-0.08243142								
ε_p	−27.661	−18.821	−18.324	−27.769	−2.096	2.764	0.000	0.605
ε_q	−20.858	−12.018	−18.324	−27.769	−2.096	2.764	0.000	0.605
B = 0.50 a.u., S = 1, $E^{\mathrm{C,RPA}}$=-0.04192719								
ε_p	−47.374	−36.391	−21.673	−34.060	−1.273	2.583	0.093	1.403
ε_q	−10.926	−6.722	−7.337	−10.833	−0.882	0.175	0.000	−0.707

obvious. The quasiparticle energies of both electrons as well as R^{C}_q and I^{C}_q become completely independent of each other. In this case, clearly the TRS breaking ansatz outlined in Sec. 2 is required.

4.2 Validation of correlation energies for time-reversal symmetry breaking systems

To validate and test the implementation of the RPA correlation and *GW* self-energies, the algorithm outlined in Sec. 2.2 is tested against reference solutions. Canonical N^6 scaling implementations, employing the spectral solution for the *GW* correlation self-energies have been outlined in Refs. 11 and 12. As these implementation extract all excited states, also the canonical RPA energies can be extracted from them by simply applying Eq. 2.

As model system for an open-shell system with strong SOC, an anionic Pt_6^- cluster is used.[73] The most stable structure of Pt_6^- reported in Ref. 73 is considered. As Kohn–Sham reference, the TMHF functional is used, in combination with the dhf-TZVP-2c basis set,[74] which includes ECPs with suitable spin-orbit parameters.[75] While treating six platinum atoms seems trivial, it is stressed that to obtain the spectral solution, a complex eigenvalue problem of dimension 117502 needs to be solved. Storing a single copy of the matrix takes up 211 gigabytes of memory, where at least two copies need to be stored. To determine an optimal number of integration points, the calculation for Pt_6^- is repeated using 16-256 integration points on a Gauss-Legendre grid. The obtained errors for the RPA correlation energy as well as the correlation self-energies for the HOMO and LUMO are given in Tab. 2.

Tab. 2 indicates that 64 Gauss-Legendre points are basically enough to obtain the correlation energy with a target accuracy of 10^{-8} hartree. The latter value is chosen as it is well below the error introduced by the RI approximation. This in line with the observations of Eshuis *et. al.* in their initial work, who concluded that 64 points was an optimal compromise between accuracy and efficiency.[76] The *GW* correlation self-energy is more sensitive to the integration grid, with the HOMO only converging to the target accuracy of 10^{-3} eV when 256 points on a Gauss-Legendre grid are being used. The LUMO seems to be less demanding, converging rapidly with the number of integration points, reaching target accuracy at the same rate as the RPA correlation energy. Again, the target accuracy is chosen to be well below the error of the RI approximation, which was found to be one order of magnitude larger for correlation self-energies obtained from the *GW* approximation.[9] Therefore, it is suggested to use at least 128, better 256, integration points to evaluate Eqs. 21 and especially 26. At this point it shall be noted that solving Eq. 3 for this problem takes roughly 96 hours using all 24 core of an Intel Xeon Gold 6248R processor. Contrary, solving Eq. 21 for Pt_6^- takes 2-5 minutes, depending on the number of integration points used for the numerical integration. A minimal speedup of approx. 28000 is therefore obtained with the subspace algorithm, drastically outlining the impact of reducing the scaling by two orders of magnitude for complex TRS breaking KS references.

Table 2: Deviation of the RPA correlation energy and G_0W_0 correlation self-energies of HOMO and LUMO evaluated using Eqs. 21. and 25. The reference RPA correlation energy and G_0W_0 correlation self-energies are obtained from the spectral representation, i.e. Eq. 2. The reference RPA correlation energy is -3.55216960 hartree.

Points	$\Delta\,\mathrm{E}^{\mathrm{RPA}}_{\mathrm{C}}$	$\Sigma^{\mathrm{H}}_{\mathrm{C}}$	$\Sigma^{\mathrm{L}}_{\mathrm{C}}$
16	$2.99{\cdot}10^{-6}$	1.964	-1.267
32	$3.95{\cdot}10^{-7}$	1.973	-1.232
64	$<10^{-8}$	1.997	-1.233
128	$<10^{-8}$	2.010	-1.233
256	$<10^{-8}$	2.008	-1.233
Ref.	0.0	2.008	-1.233

To further test the validity of the chosen parameters and the implementation, the RPA correlation energies and the *GW* correlation self-energies are calculated for a set of 36 molecules outlined in Ref. 12 in an external magnetic field of 1000 tesla. The magnetic field is aligned along the z-axis using the geometries provided in Ref. 77. The same functional and basis set, PBE0 and def2-TZVP, are used for consistency, combined with 256 integration points. The statistical error of the RI-RPA correlation energies when compared to the spectral solution is negligible. A root-mean-square deviation of $2.1{\cdot}10^{-7}$ hartree is found, with a maximum error of $6.1{\cdot}10^{-7}$ hartree. The obtained contour-deformation based RI-G_0W_0 correlation self-energies do not exceed the error threshold of 1 meV in all cases when compared to results from the spectral solution. A detailed listing of all values can be found in the supporting information.

4.3 Application of the random phase approximation to the spin states of [Mn(taa)] in magnetic fields

The manganese complex [Mn(pyrol)$_3$(tren)],[32] labelled [Mn(taa)], was one of the first complexes explicitly shown to undergo a spin state transition in magnetic fields.[32,33] The spin state transition and change of connected properties of this complex have since been subject to several experimental investigations.[33,78–81] It is therefore educational to investigate the theoretical behavior of this system in a magnetic field. Fig. 1 outlines the ground state energies of the approximately collinear states of [Mn(taa)] with $S_z = 1$ and $S_z = 2$ in a magnetic field of $\pm$0-150 tesla aligned along the z-axis, as well as the energy of the fully relaxed non-collinear state. Note that the energy difference between the low-spin $S_z = 1$ and the high-spin $S_z = 2$ state in the field free limit has been estimated to be 48 Kelvin (0.399 kJ/mol) from experimental data.[33] An estimate is necessary, as neither DFT nor the RPA are capable of quantitatively describing this small energy gap between the two spin states. Such a shallow gap may even be ill described using the "gold standard" coupled-cluster singles, doubles and perturbative triples CCSD(T) method.

Fig. 1 outlines that if the molecule is suitably aligned, i.e. with the z-axis along the Jahn–Teller distorted axis,,[81] the behavior of the ground state energy in a magnetic field ranging from $\pm$0-150 tesla oriented along the z-axis yields the expected near-ideal behavior. The dependence of the ground state energy on the magnetic field can then be estimated using the Zeeman effect,

$$\Delta E(B) = \vec{\mu} \cdot \vec{B}, \tag{34}$$

as outlined in Fig. 1. The optimal behavior obtained from the Zeeman effect is outlined by black lines in Fig. 1. The latter are hardly visible, as deviations of the actually calculated curves from this optimal behavior are vanishing for the approximately collinear states. As expected, the high-spin $S_z = 2$ state crosses the $S_z = 1$ state at some point if the field vector chosen to be the {0,0,-1}. The field strength at which the spin state transition occurs then mainly depends on the energy difference between these two levels. If the magnetic field vector is inverted to {0,0,1}, the ground state of the molecule is accordingly destabilized, and the $S_z = 2$ state destabilizes faster than the $S_z = 1$ state. Therefore, these states would never cross, and no spin state transition would occur. However, full non-collinear relaxation of the KS reference reveals that the true KS ground state is actually stabilized even with the magnetic field vector aligned along the {0,0,1} direction. DFT results confirm that this state still has four unpaired electrons, corresponding to the high-spin state. The difference in the relative field dependence between KS-DFT and RPA is small for this non-collinear state, but not vanishing as for the other lines. Still, the magnetic field-dependent energy shift of this state is dominated by the interaction of the electron spin with the external magnetic field. Correlation effects seemingly only play a minor role for the [Mn(taa)] complex in the comparably weak magnetic fields investigated in this section. This can however not be stated *a priori*, and it has been shown that correlation effects become more important in stronger magnetic fields.[82] For [Mn(taa)] it can be concluded that, at least for the moderate field strengths involved in switching the spin state, DFT is working correctly concerning the relative energy shifts in a magnetic field. As shown in Ref. 83, standard DFT exchange-correlation approximations tend to be well behaved also in stronger magnetic fields, though it is not known if this may change in certain situations. The RPA can then provide a convenient way to perform a simple plausibility check. The reasonable computational scaling of N^4 will keep it applicable to molecular systems of significant size. Furthermore, KS-DFT is known to be troublesome for certain kinds of molecular interactions, as e.g. dispersion interactions, for which the RPA works reasonably well. As magnetic fields have been shown to be able to propagate novel bonding mechanisms,[84] the RPA will also provide a convenient route to check DFT in case that gold standard coupled cluster methods are computationally too involved for the system of interest.

4.4 Application of contour-deformation GW to Ln(III) ions

In this section, the ionization energies of the trivalent lanthanoids Ce^{3+} to Yb^{3+} will be investigated using the non-time-reversal symmetric variant of the contour-deformation based *GW* method outlined in Sec. 2.3. Initially, the dependence on the chosen basis set size will be investigated. As KS reference, the TMHF functional will be used, as local-hybrids have been shown to perform excellent for *GW* calculations.[59] Furthermore, TMHF was already successfully applied to other properties of trivalent lanthanoid complexes with excellent results, especially when compared to other density functional approximations.[56] The obtained ionization energies are listed in Tab. 3.

Table 3: Ionization energies of trivalent lanthanoids, calculated using G_0W_0 and ev*GW* at a TMHF KS reference at the given basis set size. Experimental values taken from Refs. 85 and 86. Root-mean square (RMS), standard (SD), and maximum absolute (Max.) deviations additionally listed. All values in eV.

	TZVPP		QZVPP		Ref.
Ion	G_0W_0	ev*GW*	G_0W_0	ev*GW*	exp.
Ce^{3+}	35.38	35.76	36.02	36.45	36.91
Pr^{3+}	37.60	37.80	38.17	38.42	39.00
Nd^{3+}	39.00	39.67	39.56	40.27	40.60
Pm^{3+}	39.49	40.14	40.03	40.74	41.17
Sm^{3+}	40.04	40.66	40.55	41.23	41.64
Eu^{3+}	41.41	42.00	41.91	42.57	42.94
Gd^{3+}	42.76	43.55	43.23	44.06	44.44
Tb^{3+}	37.78	38.35	38.34	39.00	39.33
Dy^{3+}	40.28	40.23	40.82	40.86	41.23
Ho^{3+}	40.88	41.72	41.40	42.31	42.52
Er^{3+}	40.66	41.49	41.18	42.08	42.42
Tm^{3+}	40.89	41.75	41.39	42.33	42.41
Yb^{3+}	41.90	43.01	42.36	43.55	43.61
RMS	1.56	0.94	1.04	0.36	
SD.	0.20	0.17	0.22	0.14	
Max.	1.76	1.20	1.25	0.58	

For the Ln^{3+} ions, the choice of basis set is crucial. Using the triple-ζ x2c-TZVPPall-2c basis set leads to unacceptable large root-mean-square (RMS) deviations of 1.76 and 1.20 eV for G_0W_0 and ev*GW* respectively. While ev*GW* significantly outperforms G_0W_0, both are unsuitable for determining the ionization potential of lanthanoid ions when combined with a triple-ζ basis set. Switching to the larger quadruple-ζ x2c-QZVPPall-2c basis set significantly lowers the errors obtained for the IEs of the Ln^{3+} ions, providing results comparable to the standard errors of the *GW* method.[87] Especially ev*GW*@TMHF combined with the x2c-QZVPPall-2c method is able to reliably predict the IEs for the whole series. Therefore, ev*GW* should be preferred over G_0W_0 when treating lanthanoids within the *GW* method. The choice of basis sets gains significant importance compared to standard *GW* calculations. Only quadruple-ζ basis sets provide sufficient flexibility to yield converged *GW* quasiparticle energies. ev*GW* com-

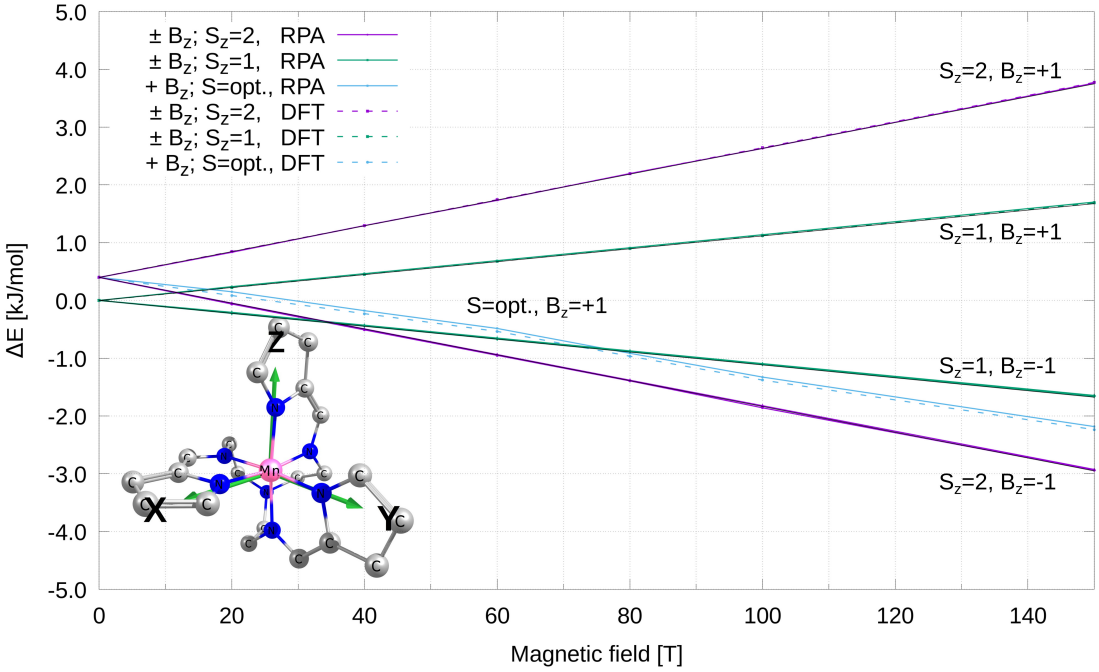

Figure 1: Magnetic field dependence of the $S = 1$ and $S = 2$ states of [Mn(taa)]. The magnetic field vector is aligned along the {0,0,1} (positive energy branches, $B_z = +1$) and {0,0,-1} (negative energy branches, $B_z = -1$) vector. Magnetic field strength is varied from 0 to 150 tesla. $S_z = 1$ and $S_z = 2$ denote the approximately collinear states, while S=opt denotes the lowest energy non-collinear Kohn–Sham state for the $B_z = +1$ branch. For the $B_z = -1$ branches, the collinear solutions are the lowest energy solutions. Energy difference between the $S_z = 1$ and $S_z = 2$ has been estimated as 48 Kelvin (0.399 kJ/mol) from experimental data.[33]

bined with a flexible basis set is therefore a viable choice to tackle the electronic structure of lanthanoids.

To further investigate the performance of ev*GW*, the dependence on the reference density functional is outlined in Fig. 2. The lines representing ev*GW*@TMHF and ev*GW*@TPSSh combined with the quadruple-ζ basis set closely follow the experimental references, with RMS and standard deviations of 0.36/0.40 and 0.14/0.17 eV respectively. It is interesting to note that the error for these two functionals nearly monotonically reduces as the nuclear charge Z grows, with the largest errors found for Ce^{3+} and Pr^{3+}, and the lowest ones for Tm^{3+} and Yb^{3+}. No such trend is observed for ωB97M and PBE0. The ωB97M and PBE0 references feature larger RMS deviations, but slightly lower standard deviations, hinting at a more linear offset compared to the experimental results. Overall, if combined with the large quadruple-ζ basis set, the deviations of ev*GW* quasiparticle energies for trivalent lanthanoids is not larger than the general error observed for the *GW* approximation.[88] Starting point dependence is significant, but again comparable to standard non-relativistic *GW* methods.[57]

4.5 Application of the contour-deformation based evGW-BSE method to selected Ln^{3+} ions

Given the excellent performance of TMHF for the IEs of lanthanoids, it is also interesting to check the performance for the combined ev*GW*-Bethe–Salpeter equation (BSE) method for optical excitations. While applying the BSE to the quasiparticle states of the ev*GW* calculations outlined in the Sec. 4.4 will yield a set of excited states, the viability of this approach needs to be discussed first. For wavefunction based methods, the generalized 2c and 4c Hartree-Fock references are sub-optimal starting points for calculating excited states of trivalent lanthanoids, severely hampering standard equation-of-motion or linear response based coupled-cluster schemes. This is due to the artificial breaking of time-reversal symmetry in the HF reference state due to the single-determinant ansatz.[25] To resolve this issue, multi-reference methods as e.g. complete-active space (CAS) methods have been employed within a relativistic framework. This however severely limits the number of accessible molecular systems, as relativistic CAS-SCF or multireference configuration interaction (CI) calculations quickly become intractable for more than a few atoms. KS references suffer from the same issue, artificially breaking time-reversal symmetry due to their single-determinant nature. Neither time-dependent DFT nor the *GW*-BSE ansatz can repair this initial fault of the KS reference. Therefore, degenerate states may not be recovered as such. Instead, this will lead to an artificial state splitting, which strictly has to be kept in mind when performing *GW*-BSE calculations for trivalent lanthanoid ions, or any other KS reference that artificially breaks time-reversal symmetry. Curiosity and the technical importance of lanthanoid ions however justifies a closer investigation of the performance of the *GW*-BSE method on these systems. The europium(III) ion is often of special interest, given its intense $^5D \rightarrow {}^7F$ emission. As Eu^{3+} also features a non-degenerate $^7F_0$ ground state, it is among least problematic Ln^{3+} ions for single-determinant methods. Still, with several low-lying excited states, Eu^{3+} is a demanding case. Furthermore, Tb^{3+} and Yb^{3+} are also interesting species in optical applications, either providing a modulated variant of the Eu^{3+} emission lines (Tb^{3+}), additionally stimulating light emission,[89] or emitting light in the near-infra red region (Yb^{3+}). The latter two feature non-degenerate ground states, adding considerable strain to the *GW*-BSE method. Additionally, Yb^{3+} features an odd number of unpaired electrons, adding further complexity to the system. Tab. 4 lists the excited states of these three ions assessed using the ev*GW*-BSE method.

The performance of ev*GW*-BSE is respectable, leading to qualitatively correct results for all underlying functionals. ev*GW*-BSE is able to reproduce the $^7F_0 \rightarrow {}^7F_J$ transition of Eu^{3+}, though especially the three lowest state are very sensitive to the chosen pa-

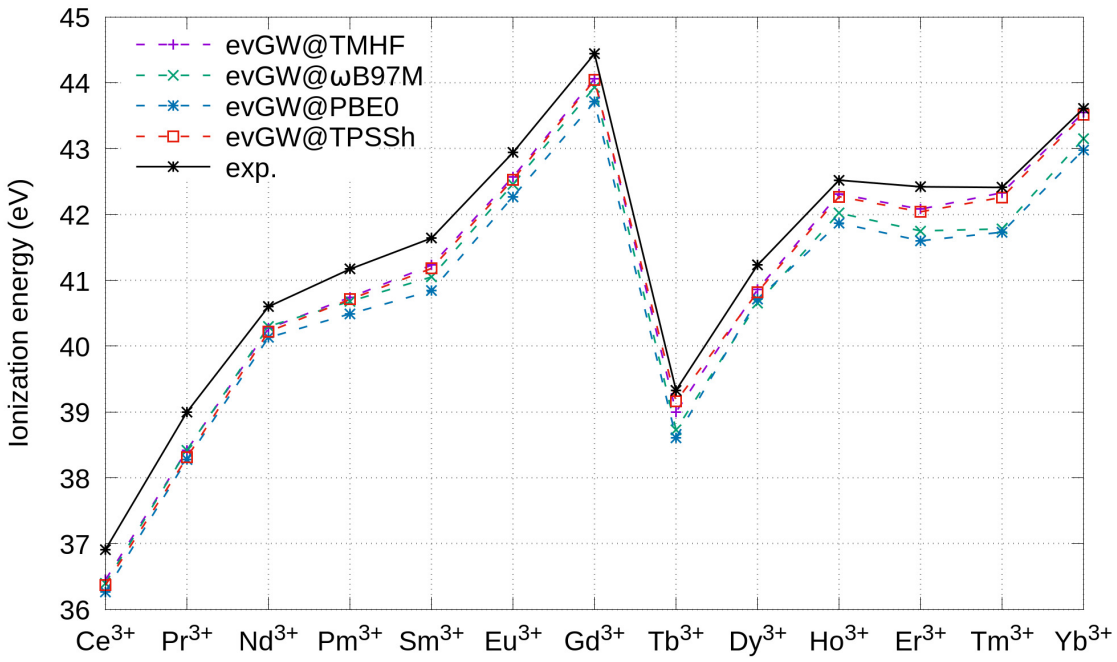

Figure 2: Trend of ionization energies (in eV) for the trivalent lanthanoid ions Ln^{3+}, calculated using ev*GW*@DFT and the x2c-QZVPPall-2c basis set.

Table 4: Energy levels of the lowest excited states of Eu^{3+}, Tb^{3+}, and Yb^{3+} for various ev*GW*-BSE@DFT methods. All calculations use the x2c-QZVPPall-2c basis set. All values in cm^{-1}.

		ev*GW*@DFT-BSE				
atom	state	TMHF	ωB97M	PBE0	TPSSh	Ref.
Eu^{3+}	$^7F_1$	671	169	122	690	370
	$^7F_2$	709	1316	399	732	1040
	$^7F_3$	856	1472	994	801	1890
	$^7F_4$	2548	1678	1388	2370	2860
	$^7F_5$	3542	2667	2568	3443	3910
	$^7F_6$	5651	4307	4230	5229	4948
	$^5D_0$	16953	16679	15381	17298	17270
	$^5D_1$	17909	18360	17587	17987	19030
	$^5D_2$	20795	21703	21278	21017	21510
Tb^{3+}	$^7F_5$	1449	873	1038	1148	2052
	$^7F_4$	1868	1714	1924	1529	3314
	$^7F_3$	5006	4494	4628	1907	4292
	$^7F_2$	5065	4781	4889	2502	4977
	$^7F_1$	7104	6093	6164	2919	5432
	$^7F_0$	7241	7133	6999	5483	5654
	$^5D_4$	18582	19740	19068	18164	20454
Yb^{3+}	$^2F^a_{7/2}$	4140	3619	3583	3962	0
	$^2F^a_{5/2}$	13857	14369	14497	14115	10214
	diff.	9717	10750	10913	10153	10214

a) assessed as the difference of the centers of mass of the $^2F_{7/2}$ and $^2F_{5/2}$ states.

rameters of the underlying calculation. The $^7F_0 \rightarrow {}^5D_J$ transitions depend to a lesser extend on the underlying functionals, with the kinetic-energy density dependent functionals TMHF, ωB97M, and TPSSh yielding rather similar results. The latter are in very good agreement with the experimental reference results. Only PBE0 deviates significantly for the $^7F_0 \rightarrow {}^5D_0$ transition. Most importantly, the results outlined in Tab. 4 demonstrate that ev*GW*-BSE is able to predict even excitations within the $4f$ manifold of Eu^{3+} reliably. Accuracy is comparable to complete active space approaches,[90,91] at a significantly reduced cost. ev*GW*-BSE results for Tb^{3+} yield a similar picture, with slightly raised errors. For the $4f^6$ and $4f^8$ ions, the gap between the ^7F and ^5D manifolds is correctly reproduced. The important $^7F_2 \rightarrow {}^5D_0$ transition of Eu^{3+} has a predicted excitation energy of 16097 cm^{-1} for ev*GW*-BSE@TMHF, which deviates by only 717 cm^{-1} from the experimental reference results. Errors are not larger than generally expected from ev*GW*-BSE, with deviations being in the range of 1000-2000 cm^{-1}. Therefore, it is worth to try reproducing more complex spectra involving Eu^{3+}. These results come with one important limitation. As mentioned before, ev*GW*-BSE is not able to reproduce the degeneracy of the respective states. Only a single component of each excited state is found, representing the respective $4f_{\mathrm{occ}} \rightarrow 4f_{\mathrm{LUMO}}$ (Eu) and $4f_{\mathrm{HOMO}} \rightarrow 4f_{\mathrm{virt}}$ (Tb) excitations. Therefore, only 6 excited states are extracted, contrary to the expected 48 states. The missing 42 excited states are located at considerably higher energies, many eV above the ground state. While ev*GW*-BSE was expected to fail to display the correct degeneracy behavior, the large shift of the remaining 42 states is surprising. This large deviation can be attributed to the inability of KS-DFT to describe degenerate atomic states with different magnetic quantum numbers.[62,92] This deficiency cannot be repaired by the perturbation theory based *GW* corrections used in this manuscript. Instead, density functionals that correct this issue as well as possible within a single-determinant ansatz need to be developed. Such a hypothetical density functional would be required to correctly react to the current density, to account for current-carrying states. Further, this functional should have a strong correlation component involved. Unfor-

tunately, no density functional approximation yet developed fulfills both requirements with the required accuracy.

For the Yb^{3+} ion, featuring a $4f^{13}$ configuration, an artificial crystal field splitting of the $^2F_{5/2}$ and $^2F_{7/2}$ states is observed, which is on the order of a few thousand cm^{-1}. Calculating the center-of-mass, the energy difference can nevertheless be obtained quite reliably from ev*GW*-BSE for all tested density functionals. When the dominant contributions are analyzed in detail for the rather simple Yb^{3+} spectrum, it can be concluded that the excitations to the excited $^2F_{7/2}$ manifold are again characterized by a single transition from an occupied $4f$ spinor to the single unoccupied $4f$ spinor. Excitations within the $^2F_{5/2}$ manifold are generally more complex, as the ground state itself belong to that manifold. Indeed, this is reflected in the error of the splitting in the degenerate states. For ev*GW*-BSE@TMHF, the splitting between the $^2F_{5/2}$ levels is only about $2000cm^{-1}$, while the $^2F_{7/2}$ levels are split by 4000 cm^{-1}, with the ground state being an additionally 3000 cm^{-1} below the first excited state. Similar effects as for Yb^{3+} have been observed for U^{5+} in Ref. 25 for time-dependent HF and DFT. The latter features a $5f^1$ configuration, yielding an energetic inversion of the $^2F_{5/2}$ and $^2F_{7/2}$ states, with the same splitting pattern otherwise. It is further noted that these artificial splittings are generally observed for systems with an unpaired number of electrons in single-determinant methods, not being limited to f shells.[93] The center-of-mass of the splitted states still aligns well with experimental findings, but the usability in actual complexes will be severely limited in these cases. Once the issues concerning artificial splittings are sorted out, the errors obtained from the 2c TRS breaking *GW*-BSE method are again not larger than the error obtained for its non-relativistic counterpart.[94] Starting point dependence is moderate, with the local hybrid TMHF performing consistently well.

4.6 Application of evGW-BSE to a Eu^{3+} complex

Ref. 66 presents an interesting complex that emits circular polarized light stemming from a $^5D \rightarrow {}^7F$ emission line. By cutting the linking unit, a single active Eu^{3+} site is isolated. In the resulting complex, outlined in Fig. 3, three pyridine-2,6-dicarboxylic amine (PDCA) molecules coordinate a Eu^{3+} center.

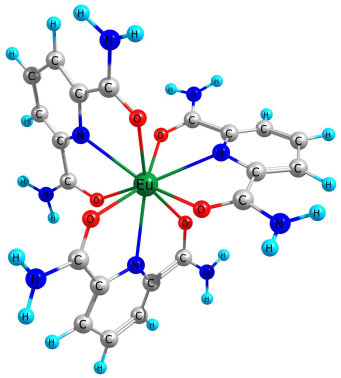

Figure 3: Structure of $[Eu(PDCA)_3]^{3+}$ optimized using the 1c-X2C-r^{2}SCAN density function in conjunction with the x2c-QZVPPall-2c (Eu) and x2c-TZVPPall-2c (others) basis set.

The resulting $[Eu(PDCA)_3]^{3+}$ complex features a nine-fold coordinated europium atom in an approximately C_3-symmetric environment. Fig. 4 shows the calculated ev*GW*-BSE@TMHF absorption spectrum of the $^7F_0$ ground state of the complex.

Main peaks can be found at 1.88 eV, 2.40 eV, 3.48 eV, and 3.80 eV. The first two excitations, being in the visible range, can clearly be identified as $f-f$ transitions from the NTO pairs. The peak at 1.88 eV likely represents the principal $^5D_0 \rightarrow {}^7F_0$ excitation, with subsequent ^5D_J states following. This corresponds to a shift of 0.22 eV of this excitation when compared to the free ion calculations. This introduced error can likely be attributed to the limited space of quasiparticle states treated in the ev*GW* refinement, as only a subset of 40 spinors can be kept active in the ev*GW* quasiparticle step. Nevertheless, the principal experimental absorption spectrum outlined in Ref. 66 is well reproduced. Experimentally, intra-ligand excitation peaks are observed at 3.52 eV and 4.05 eV, with the corresponding calculated peaks being located at 3.48 and 3.80 eV in the ev*GW*-BSE calculation. These excitations are strongly centered on the ligands, as outlined by their leading natural transition orbitals (NTOs), depicted as insets of Fig. 4. The absorption spectrum of the $^7F_0$ ground state of the $[Eu(PDCA)_3]^{3+}$ complex can therefore be decomposed into two parts: That of the central europium(III) ion, and that of the ligand shell. Unfortunately, starting from the $^7F_0$ state, the oscillator strengths or related quantities of the $^5D_0 \rightarrow {}^7F_J$ transitions with $J \neq 0$ cannot be obtained directly. Using the maximum overlap method (MOM), however the $^5D_0$ excited state of the of the $[Eu(PDCA)_3]^{3+}$ complex can be converged. The "projected initial-state MOM" (PIMOM) method was found to be particularly effective for this task.[95] As starting point for the PIMOM approach, the scalar-relativistic ^5D state was chosen, from which the TMHF calculation converged smoothly to the desired excited state. The ev*GW*-BSE@TMHF spectrum of the corresponding excited state is shown in Fig. 5.

Starting from the $^5D_0$ state, the principal $^5D_0 \rightarrow {}^7F_0$ emission line can be found at 2.43 eV, being blue-shifted by approximately 0.33 eV when compared to the free ion. Again, this error is attributed to the limited number of quasiparticle states corrected within the ev*GW* procedure, and additionally to the more complex (and erroneous) way of obtaining the Kohn–Sham reference of the excited state. Unfortunately, this also outlines that error cancellation is of little help for the ev*GW*-BSE method when applied to such electronically complicated systems. Nevertheless, starting from the $^7F_0$ state, the sequence of ^7F_J states is well reproduced. They approximately span a range of 0.89 eV, corresponding to 7180 cm^{-1}, slightly larger than the span of 0.62 eV which is found experimentally. The oriented rotator strength,[96] which is tightly connected to circular dichroism,[97] hints at the $^5D_0 \rightarrow {}^7F_1$ being especially active in that respect, in line with experimental observations and the general assumption the this emission line has a large magnetic component.[98] The calculated lifetimes of the de-excitations shown in Fig. 5 range from 1 to 5 milliseconds. This is again in very good agreement with the experimental results of Ref. 66, where a lifetime of 1.6 milliseconds is observed for the main emission line. The sign change of the circular dichroism signal after the $^5D_0 \rightarrow {}^7F_1$ peak is correctly reproduced. Furthermore, Fig. 5 indicates that excitations from or to the $^5D_0$ state are also more likely to transfer charge between the central Eu atom and the ligand. NTO analysis of the low-lying excitations reveals a significant contribution of ligand orbitals for the excitations at 0.45 eV and 0.95 eV. Such contributions are not observed for excited states starting from the ^7F ground state at all. Compared to the ev*GW*-BSE calculations performed on atomic Eu^{3+}, it is interesting to note that the artificially large splitting of the ^7F_J states is largely gone, though many of the states exhibit a vanishing oscillator or rotator strength and are therefore not visible in Fig. 5. The loss of symmetry lifts any degeneracy, making the electronic structure more accessible for standard single-determinant KS based density functional approximations. The quasiparticle spectrum is significantly narrowed, and only a slightly too large crystal field splitting remains as outlined in Fig. 5. This is a remarkable result. The main deficiency is now that the ev*GW* quasiparticle treatment can only be carried out for a lim-

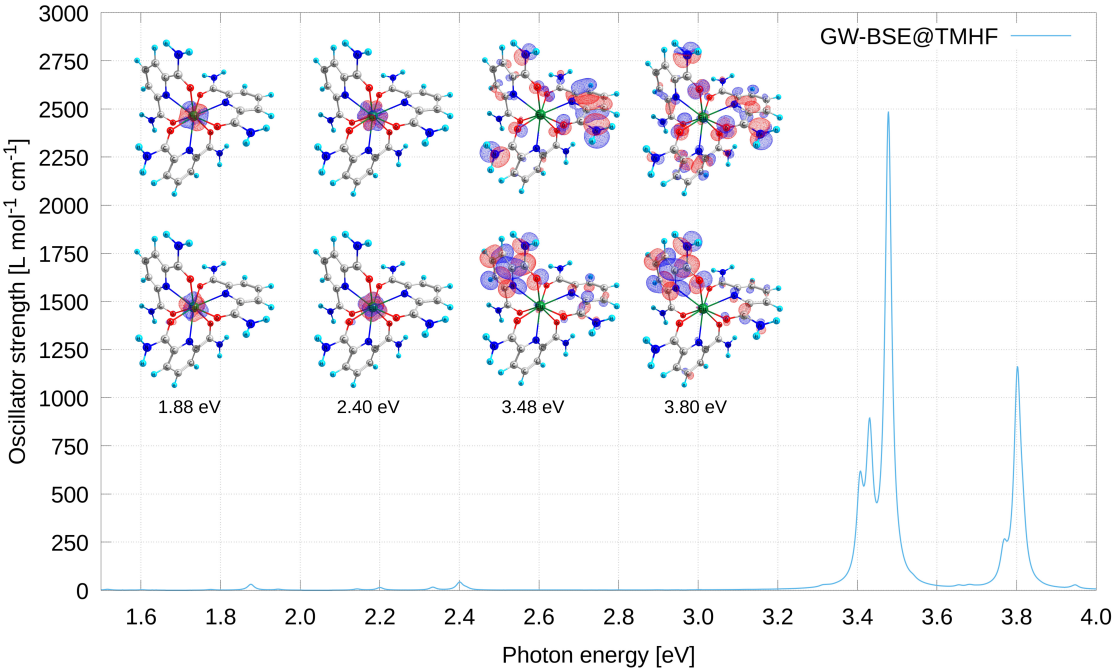

Figure 4: Optical absorption (oscillator strength) spectrum of $[Eu(PDCA)_3]^{3+}$, calculated using 2c ev*GW*-BSE@TMHF and the x2c-QZVPPall-2c/x2c-TZVPPall-2c (Eu/other atoms) basis set. The insets show the leading hole (upper) and particle (lower) NTOs for the most prominent excitations. An isovalue of 0.04 has been used to generate the NTO plots.

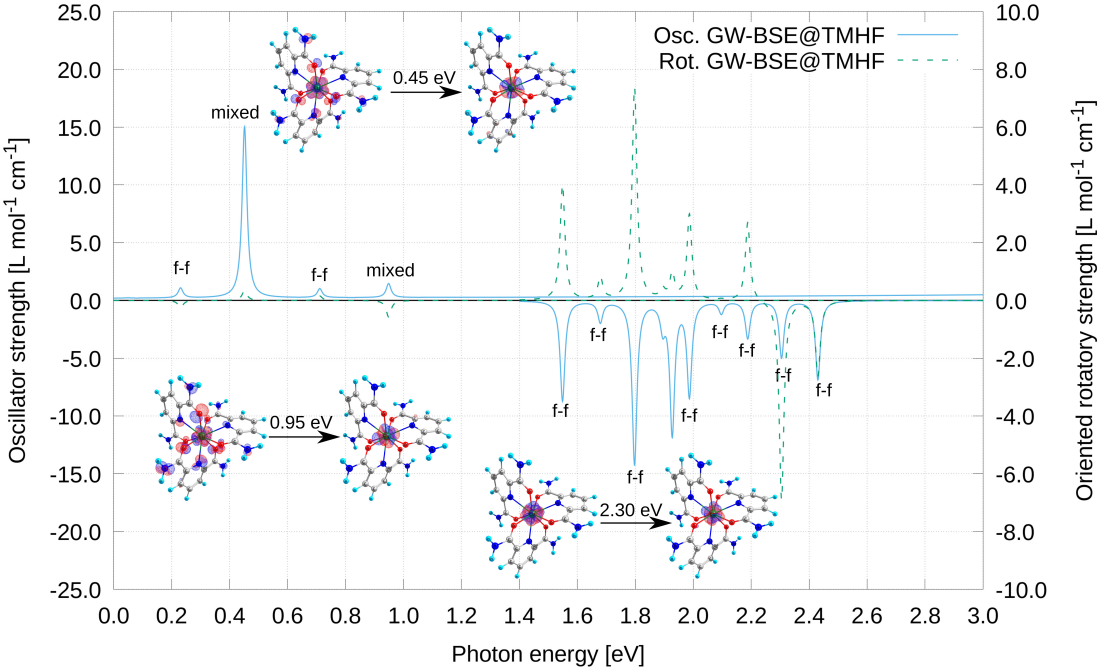

Figure 5: Optical absorption (oscillator strength) and circular dichroism (oriented rotator strenght) spectra of the $^5D_0$ excited state of $[Eu(PDCA)_3]^{3+}$, calculated using 2c ev*GW*-BSE@TMHF and the x2c-QZVPPall-2c/x2c-TZVPPall-2c (Eu/other atoms) basis set. The insets show the leading hole and particle NTOs for the most prominent peaks. An isovalue of 0.04 has been used to generate the NTO plots.

ited range of spinors before calculations becoming intractable. In this example, the spinors 300-339 where corrected using the ev*GW* method, which took approximately 3 days using a single NVIDIA A100 GPU. The remaining spinors were shifted accordingly. Increasing the range of active spinors would also increase the overall quality of results, but the evaluation of Eq. 27 becomes increasingly demanding for states far away from the Fermi level as more and more contours need to be calculated. Correcting all 3246 spinors (or even 100 spinors around the Fermi level) is therefore currently impossible. More efficient schemes of evaluating Eq. 25 need to be developed and adapted to the two-component formalism.

5 Conclusion

A canonical auxiliary subspace formulation of the correlation energy in the random phase approximation as well as the correlation self-energy in the *GW* approximation based on the resolution-of-the-identity approximation valid for time-reversal symmetry breaking HF and KS references has been outlined. Compared to the spectral variants based on the plasmon formula, the scaling of the subspace-RI variants is reduced by at least two orders of magnitude, in combination with a largely reduced prefactor. This leads to drastic speedups, enabling the application of the RPA and the *GW* method to TRS breaking KS references with a few thousand basis functions. Introduced errors are negligible when a suitable integration grid is chosen. For the latter, 256 points on a Gauss–Legendre grid have been proven to yield fully converged results. Using the reformulation of the RPA, the spin state transition of the well-known [Mn(taa)] complex was investigated, proving that electron correlation only plays a minor role in the behavior of this complex in a magnetic field. Furthermore, it could be shown that the *GW*-BSE method is able to describe light-matter interactions for the electronically highly involved lanthanoids, and can even be used to investigate corresponding molecular systems with lanthanoid centers. While certain drawback stemming from the single-determinant KS reference cannot be resolved by the RPA and *GW* method, the results outlined in Sec. 4 are very encouraging. For example, it could be shown that the $^5D_0$ state of Eu^{3+} is more likely to participate in ligand-metal charge transfer compared to the $^7F_0$ state. Given the combination of broad applicability and reasonable computational cost of the outlined method, they will provide useful tools for the frontiers of theoretical chemistry and physics. They allow for a description of complex molecular systems, including magnetic fields and relativistic effects, at a reasonable timescale. Combined with the recently developed *GW*-BSE damped response ansatz,[47] furthermore relativistic open-shell systems or systems in finite fields can be simulated in optical multiscale simulations, opening novel possibilities to the field of *in silico* optical material design.[99]

6 Supporting Information

Reference and auxiliary subspace based RPA correlation energies and G_0W_0 correlation self-energies for 36 small organic molecules at 1000 tesla, detailed RPA and PBE0 energies of [Mn(taa)] from 0 to 150 tesla, ev*GW* quasiparticle energies for trivalent lanthanoid ions, and the optimized structures of [Mn(taa)] ($S = 1$ and $S = 2$ states) and $[Eu(PDCA)_3]^{3+}$ in xyz format can be found in the supporting information.

Acknowledgement C. H. gratefully acknowledges funding by Volkswagen Stiftung. Furthermore, C. H. thanks Yannick Franzke, Carsten Rockstuhl, and Wim Klopper for fruitful discussions and ongoing support over the years, enabling this project.

References

(1) Bohm, D.; Pines, D. A Collective Description of Electron Interactions. I. Magnetic Interactions. *Phys. Rev.* **1951**, *82*, 625–634.

(2) Pines, D.; Bohm, D. A Collective Description of Electron Interactions: II. Collective vs Individual Particle Aspects of the Interactions. *Phys. Rev.* **1952**, *85*, 338–353.

(3) Bohm, D.; Pines, D. A Collective Description of Electron Interactions: III. Coulomb Interactions in a Degenerate Electron Gas. *Phys. Rev.* **1953**, *92*, 609–625.

(4) Furche, F. Developing the random phase approximation into a practical post-Kohn–Sham correlation model. *J. Chem. Phys.* **2008**, *129*, 114105.

(5) Ren, X.; Rinke, P.; Joas, C.; Scheffler, M. Random-phase approximation and its applications in computational chemistry and materials science. *J. Mater. Sci.* **2012**, *47*, 7447–7471.

(6) Chen, G. P.; Voora, V. K.; Agee, M. M.; Balasubramani, S. G.; Furche, F. Random-Phase Approximation Methods. *Annu. Rev. Phys. Chem.* **2017**, *68*, 421–445.

(7) Hedin, L. New Method for Calculating the One-Particle Green's Function with Application to the Electron-Gas Problem. *Phys. Rev.* **1965**, *139*, A796–A823.

(8) Aryasetiawan, F.; Gunnarsson, O. The GW method. *Rep. Prog. Phys.* **1998**, *61*, 237.

(9) van Setten, M. J.; Weigend, F.; Evers, F. The *GW*-Method for Quantum Chemistry Applications: Theory and Implementation. *J. Chem. Theory Comput.* **2013**, *9*, 232–246.

(10) Holzer, C.; Gui, X.; Harding, M. E.; Kresse, G.; Helgaker, T.; Klopper, W. Bethe–Salpeter correlation energies of atoms and molecules. *J. Chem. Phys.* **2018**, *149*, 144106.

(11) Holzer, C.; Teale, A. M.; Hampe, F.; Stopkowicz, S.; Helgaker, T.; Klopper, W. *GW* quasiparticle energies of atoms in strong magnetic fields. *J. Chem. Phys.* **2019**, *150*, 214112.

(12) Holzer, C.; Pausch, A.; Klopper, W. The GW/BSE Method in Magnetic Fields. *Front. Chem.* **2021**, *9*.

(13) Furche, F. Molecular tests of the random phase approximation to the exchange-correlation energy functional. *Phys. Rev. B* **2001**, *64*, 195120.

(14) Eshuis, H.; Yarkony, J.; Furche, F. Fast computation of molecular random phase approximation correlation energies using resolution of the identity and imaginary frequency integration. *J. Chem. Phys.* **2010**, *132*, 234114.

(15) Kaltak, M.; Klimeš, J.; Kresse, G. Low Scaling Algorithms for the Random Phase Approximation: Imaginary Time and Laplace Transformations. *J. Chem. Theory Comput.* **2014**, *10*, 2498–2507.

(16) Henderson, T. M.; Scuseria, G. E. The connection between self-interaction and static correlation: a random phase approximation perspective. *Mol. Phys.* **2010**, *108*, 2511–2517.

(17) Govoni, M.; Galli, G. Large Scale GW Calculations. *J. Chem. Theory Comput.* **2015**, *11*, 2680–2696.

(18) Scherpelz, P.; Govoni, M.; Hamada, I.; Galli, G. Implementation and Validation of Fully Relativistic GW Calculations: Spin–Orbit Coupling in Molecules, Nanocrystals, and Solids. *J. Chem. Theory Comput.* **2016**, *12*, 3523–3544.

(19) Holzer, C.; Klopper, W. Ionized, electron-attached, and excited states of molecular systems with spin–orbit coupling: Two-component *GW* and Bethe–Salpeter implementations. *J. Chem. Phys.* **2019**, *150*, 204116.

(20) Golze, D.; Wilhelm, J.; van Setten, M. J.; Rinke, P. Core-Level Binding Energies from GW: An Efficient Full-Frequency Approach within a Localized Basis. *J. Chem. Theory Comput.* **2018**, *14*, 4856–4869.

(21) Duchemin, I.; Blase, X. Robust Analytic-Continuation Approach to Many-Body GW Calculations. *J. Chem. Theory Comput.* **2020**, *16*, 1742–1756.

(22) Kühn, M. Correlation Energies from the Two-Component Random Phase Approximation. *J. Chem. Theory Comput.* **2014**, *10*, 623–633.

(23) Kühn, M.; Weigend, F. One-Electron Energies from the Two-Component *GW* Method. *J. Chem. Theory Comput.* **2015**, *11*, 969–979.

(24) Vignale, G.; Rasolt, M. Current- and spin-density-functional theory for inhomogeneous electronic systems in strong magnetic fields. *Phys. Rev. B* **1988**, *37*, 10685–10696.

(25) Kasper, J. M.; Jenkins, A. J.; Sun, S.; Li, X. Perspective on Kramers symmetry breaking and restoration in relativistic electronic structure methods for open-shell systems. *J. Chem. Phys.* **2020**, *153*, 090903.

(26) Schurkus, H. F.; Ochsenfeld, C. Communication: An effective linear-scaling atomic-orbital reformulation of the random-phase approximation using a contracted double-Laplace transformation. *J. Chem. Phys.* **2016**, *144*, 031101.

(27) Graf, D.; Beuerle, M.; Schurkus, H. F.; Luenser, A.; Savasci, G.; Ochsenfeld, C. Accurate and Efficient Parallel Implementation of an Effective Linear-Scaling Direct Random Phase Approximation Method. *J. Chem. Theory Comput.* **2018**, *14*, 2505–2515.

(28) Wilhelm, J.; Golze, D.; Talirz, L.; Hutter, J.; Pignedoli, C. A. Toward GW Calculations on Thousands of Atoms. *J. Phys. Chem. Lett.* **2018**, *9*, 306–312.

(29) Duchemin, I.; Blase, X. Separable resolution-of-the-identity with all-electron Gaussian bases: Application to cubic-scaling RPA. *J. Chem. Phys.* **2019**, *150*, 174120.

(30) Förster, A.; Visscher, L. Low-Order Scaling G0W0 by Pair Atomic Density Fitting. *J. Chem. Theory Comput.* **2020**, *16*, 7381–7399, PMID: 33174743.

(31) Wilhelm, J.; Seewald, P.; Golze, D. Low-Scaling GW with Benchmark Accuracy and Application to Phosphorene Nanosheets. *J. Chem. Theory Comput.* **2021**, *17*, 1662–1677, PMID: 33621085.

(32) Sim, P. G.; Sinn, E. First manganese(III) spin crossover, first d4 crossover. Comment on cytochrome oxidase. *J. Am. Chem. Soc.* **1981**, *103*, 241–243.

(33) Chikara, S.; Gu, J.; Zhang, X.-G.; Cheng, H.-P.; Smythe, N.; Singleton, J.; Scott, B.; Krenkel, E.; Eckert, J.; Zapf, V. S. Magnetoelectric behavior via a spin state transition. *Nat. Comm.* **2019**, *10*, 4043.

(34) Lustig, W. P.; Mukherjee, S.; Rudd, N. D.; Desai, A. V.; Li, J.; Ghosh, S. K. Metal–organic frameworks: functional luminescent and photonic materials for sensing applications. *Chem. Soc. Rev.* **2017**, *46*, 3242–3285.

(35) Beitz, J. V. Chapter 120 Similarities and differences in trivalent lanthanide- and actinide-ion solution absorption spectra and luminescence studies. In *Lanthanides/Actinides: Chemistry*; Handbook on the Physics and Chemistry of Rare Earths; Elsevier, 1994; Vol. 18; pp 159–195.

(36) Tanner, P. A.; Yeung, Y.-Y.; Ning, L. Some Aspects of Configuration Interaction of the 4fN Configurations of Tripositive Lanthanide Ions. *J. Phys. Chem. A* **2014**, *118*, 8745–8752.

(37) Dolg, M. *Computational methods in lanthanide and actinide chemistry*; John Wiley & Sons: West Sussex, United Kingdom, 2015.

(38) Leng, X.; Jin, F.; Wei, M.; Ma, Y. *GW* method and Bethe–Salpeter equation for calculating electronic excitations. *Wiley Interdiscip. Rev.: Comput. Mol. Sci.* **2016**, *6*, 532–550.

(39) Krause, K.; Klopper, W. Implementation of the Bethe-Salpeter equation in the TURBOMOLE program. *J. Comput. Chem.* **2017**, *38*, 383–388.

(40) Blase, X.; Duchemin, I.; Jacquemin, D. The Bethe–Salpeter equation in chemistry: relations with TD-DFT, applications and challenges. *Chem. Soc. Rev.* **2018**, *47*, 1022–1043.

(41) Gui, X.; Holzer, C.; Klopper, W. Accuracy Assessment of *GW* Starting Points for Calculating Molecular Excitation Energies Using the Bethe–Salpeter Formalism. *J. Chem. Theory Comput.* **2018**, *14*, 2127–2136.

(42) Blase, X.; Duchemin, I.; Jacquemin, D.; Loos, P.-F. The Bethe–Salpeter Equation Formalism: From Physics to Chemistry. *J. Chem. Phys. Lett.* **2020**, *11*, 7371–7382.

(43) Pausch, A.; Klopper, W. Efficient evaluation of three-centre two-electron integrals over London orbitals. *Mol. Phys.* **2020**, *118*, e1736675.

(44) Langreth, D. C.; Perdew, J. P. Exchange-correlation energy of a metallic surface: Wave-vector analysis. *Phys. Rev. B* **1977**, *15*, 2884–2901.

(45) Henderson, H. V.; Searle, S. R. On Deriving the Inverse of a Sum of Matrices. *SIAM Review* **1981**, *23*, 53–60.

(46) Oschlies, A.; Godby, R. W.; Needs, R. J. GW self-energy calculations of carrier-induced band-gap narrowing in n-type silicon. *Phys. Rev. B* **1995**, *51*, 1527–1535.

(47) Kehry, M.; Franzke, Y. J.; Holzer, C.; Klopper, W. Quasirelativistic two-component core excitations and polarisabilities from a damped-response formulation of the Bethe–Salpeter equation. *Mol. Phys.* **2020**, *118*, e1755064.

(48) Franzke, Y. J.; Holzer, C.; Mack, F. NMR Coupling Constants Based on the Bethe–Salpeter Equation in the *GW* Approximation. *J. Chem. Theory Comput.* **2022**, *18*, 1030–1045.

(49) Kotani, T.; Van Schilfgaarde, M.; Faleev, S. V. Quasiparticle self-consistent *GW* method: A basis for the independent-particle approximation. *Phys. Rev. B* **2007**, *76*, 165106.

(50) Balasubramani, S. G.; Chen, G. P.; Coriani, S.; Diedenhofen, M.; Frank, M. S.; Franzke, Y. J.; Furche, F.; Grotjahn, R.; Harding, M. E.; Hättig, C.; Hellweg, A.; Helmich-Paris, B.; Holzer, C.; Huniar, U.; Kaupp, M.; Marefat Khah, A.; Karbalaei Khani, S.; Müller, T.; Mack, F.; Nguyen, B. D.; Parker, S. M.; Perlt, E.; Rappoport, D.; Reiter, K.; Roy, S.; Rückert, M.; Schmitz, G.; Sierka, M.; Tapavicza, E.; Tew, D. P.; van Wüllen, C.; Voora, V. K.; Weigend, F.; Wodyński, A.; Yu, J. M. TURBOMOLE: Modular program suite for *ab initio* quantum-chemical and condensed-matter simulations. *J. Chem. Phys.* **2020**, *152*, 184107.

(51) Kasper, J. M.; Li, X. Natural transition orbitals for complex two-component excited state calculations. *J. Comp. Chem.* **2020**, *41*, 1557–1563.

(52) Perdew, J. P.; Burke, K.; Ernzerhof, M. Generalized Gradient Approximation Made Simple. *Phys. Rev. Lett.* **1996**, *77*, 3865–3868.

(53) Adamo, C.; Barone, V. Toward reliable density functional methods without adjustable parameters: The PBE0 model. *J. Chem. Phys.* **1999**, *110*, 6158–6170.

(54) Tao, J.; Perdew, J. P.; Staroverov, V. N.; Scuseria, G. E. Climbing the Density Functional Ladder: Nonempirical Meta–Generalized Gradient Approximation Designed for Molecules and Solids. *Phys. Rev. Lett.* **2003**, *91*, 146401.

(55) Mardirossian, N.; Head-Gordon, M. ωB97M-V: A combinatorially optimized, range-separated hybrid, meta-GGA density functional with VV10 nonlocal correlation. *J. Chem. Phys.* **2016**, *144*, 214110.

(56) Holzer, C.; Franzke, Y. J. A Local Hybrid Exchange Functional Approximation from First Principles. *J. Chem. Phys.* **2022**, *157*, 034108.

(57) Bruneval, F.; Marques, M. A. L. Benchmarking the starting points of the *GW* approximation for molecules. *J. Chem. Theory Comput.* **2013**, *9*, 324–329.

(58) Bruneval, F.; Hamed, S. M.; Neaton, J. B. A systematic benchmark of the ab initio Bethe-Salpeter equation approach for low-lying optical excitations of small organic molecules. *J. Chem. Phys.* **2015**, *142*, 244101.

(59) Holzer, C.; Franzke, Y. J.; Kehry, M. Assessing the Accuracy of Local Hybrid Density Functional Approximations for Molecular Response Properties. *J. Chem. Theory Comput.* **2021**, *17*, 2928–2947.

(60) Treutler, O. Entwicklung und Anwendung von Dichtefunktionalmethoden. Ph.D. thesis, University of Karlsruhe (TH), Germany, 1995.

(61) Holzer, C. An improved seminumerical Coulomb and exchange algorithm for properties and excited states in modern density functional theory. *J. Chem. Phys.* **2020**, *153*, 184115.

(62) Holzer, C.; Franzke, Y. J.; Pausch, A. Current density functional framework for spin–orbit coupling. *J. Chem. Phys.* **2022**, *157*, 204102.

(63) Franzke, Y. J.; Holzer, C. Impact of the current density on paramagnetic NMR properties. *J. Chem. Phys.* **2022**, *157*, 031102.

(64) Furness, J. W.; Kaplan, A. D.; Ning, J.; Perdew, J. P.; Sun, J. Accurate and Numerically Efficient r^2SCAN Meta-Generalized Gradient Approximation. *J. Phys. Chem. Lett.* **2020**, *11*, 8208–8215.

(65) Weigend, F.; Ahlrichs, R. Balanced basis sets of split valence, triple zeta valence and quadruple zeta valence quality for H to Rn: Design and assessment of accuracy. *Phys. Chem. Chem. Phys.* **2005**, *7*, 3297–3305.

(66) Yeung, C.-T.; Yim, K.-H.; Wong, H.-Y.; Pal, R.; Lo, W.-S.; Yan, S.-C.; Yee-Man Wong, M.; Yufit, D.; Smiles, D. E.; McCormick, L. J., et al. Chiral transcription in self-assembled tetrahedral Eu_4L_6 chiral cages displaying sizable circularly polarized luminescence. *Nat. Comm.* **2017**, *8*, 1–10.

(67) Pollak, P.; Weigend, F. Segmented Contracted Error-Consistent Basis Sets of Double- and Triple-ζ Valence Quality for One- and Two-Component Relativistic All-Electron Calculations. *J. Chem. Theory Comput.* **2017**, *13*, 3696–3705.

(68) Franzke, Y. J.; Spiske, L.; Pollak, P.; Weigend, F. Segmented Contracted Error-Consistent Basis Sets of Quadruple-ζ Valence Quality for One- and Two-Component Relativistic All-Electron Calculations. *J. Chem. Theory Comput.* **2020**, *16*, 5658–5674.

(69) Franzke, Y. J.; Middendorf, N.; Weigend, F. Efficient implementation of one- and two-component analytical energy gradients in exact two-component theory. *J. Chem. Phys.* **2018**, *148*, 104410.

(70) Weigend, F. Accurate Coulomb-fitting basis sets for H to Rn. *Phys. Chem. Chem. Phys.* **2006**, *8*, 1057–1065.

(71) Hellweg, A.; Hättig, C.; Höfener, S.; Klopper, W. Optimized accurate auxiliary basis sets for RI-MP2 and RI-CC2 calculations for the atoms Rb to Rn. *Theor. Chem. Acc.* **2007**, *117*, 587–597.

(72) Rösch, N. Time-reversal symmetry, Kramers' degeneracy and the algebraic eigenvalue problem. *Chem. Phys.* **1983**, *80*, 1–5.

(73) Bumüller, D.; Yohannes, A. G.; Kohaut, S.; Kondov, I.; Kappes, M. M.; Fink, K.; Schooss, D. Structures of Small Platinum Cluster Anions Ptn–: Experiment and Theory. *J. Phys. Chem. A* **2022**, *126*, 3502–3510.

(74) Weigend, F.; Baldes, A. Segmented contracted basis sets for one- and two-component Dirac-Fock effective core potentials. *J. Chem. Phys.* **2010**, *133*, 174102.

(75) Figgen, D.; Peterson, K. A.; Dolg, M.; Stoll, H. Energy-consistent pseudopotentials and correlation consistent basis sets for the 5d elements Hf–Pt. *J. Chem. Phys.* **2009**, *130*, 164108.

(76) Eshuis, H.; Bates, J. E.; Furche, F. Electron correlation methods based on the random phase approximation. *Theor. Chem. Acc.* **2012**, *131*, 1084.

(77) Pausch, A.; Holzer, C.; Klopper, W. Efficient Calculation of Magnetic Circular Dichroism Spectra Using Spin-Noncollinear Linear-Response Time-Dependent Density Functional Theory in Finite Magnetic Fields. *J. Chem. Theory Comput.* **2022**, *18*, 3747–3758.

(78) Nakano, M.; Matsubayashi, G.-e.; Matsuo, T. Dielectric behavior of manganese(III) spin-crossover complex [Mn(taa)]. *Phys. Rev. B* **2002**, *66*, 212412.

(79) Kimura, S.; Narumi, Y.; Kindo, K.; Nakano, M.; Matsubayashi, G.-e. Field-induced spin-crossover transition of $[Mn^{III}(taa)]$ studied under pulsed magnetic fields. *Phys. Rev. B* **2005**, *72*, 064448.

(80) Sawada, Y.; Kimura, S.; Watanabe, K.; Nakano, M. High-Field Optical Spectroscopy of the Spin-Crossover Complex [MnIII(taa)]. *J. Low Temp. Phys.* **2013**, *170*, 424–429.

(81) Yu, J.-X.; Chen, D.-T.; Gu, J.; Chen, J.; Jiang, J.; Zhang, L.; Yu, Y.; Zhang, X.-G.; Zapf, V. S.; Cheng, H.-P. Three Jahn-Teller States of Matter in Spin-Crossover System Mn(taa). *Phys. Rev. Lett.* **2020**, *124*, 227201.

(82) Stopkowicz, S.; Gauss, J.; Lange, K. K.; Tellgren, E. I.; Helgaker, T. Coupled-cluster theory for atoms and molecules in strong magnetic fields. *J. Chem. Phys.* **2015**, *143*, 074110.

(83) Reimann, S.; Borgoo, A.; Tellgren, E. I.; Teale, A. M.; Helgaker, T. Magnetic-Field Density-Functional Theory (BDFT): Lessons from the Adiabatic Connection. *J. Chem. Theory Comput.* **2017**, *13*, 4089–4100.

(84) Lange, K. K.; Tellgren, E. I.; Hoffmann, M. R.; Helgaker, T. A Paramagnetic Bonding Mechanism for Diatomics in Strong Magnetic Fields. *Science* **2012**, *337*, 327–331.

(85) Sugar, J.; Reader, J. Ionization energies of doubly and triply ionized rare earths. *J. Chem. Phys.* **1973**, *59*, 2083–2089.

(86) Johnson, D. A.; Nelson, P. G. Lanthanide Ionization Energies and the Sub-Shell Break. Part 2. The Third and Fourth Ionization Energies. *J. Chem. Phys. Ref. Data* **2017**, *46*, 013109.

(87) Caruso, F.; Dauth, M.; van Setten, M. J.; Rinke, P. Benchmark of GW Approaches for the GW100 Test Set. *J. Chem. Theory Comput.* **2016**, *12*, 5076–5087.

(88) van Setten, M. J.; Caruso, F.; Sharifzadeh, S.; Ren, X.; Scheffler, M.; Liu, F.; Lischner, J.; Lin, L.; Deslippe, J. R.; Louie, S. G.; Yang, C.; Weigend, F.; Neaton, J. B.; Evers, F.; Rinke, P. *GW* 100: Benchmarking G_0W_0 for molecular systems. *J. Chem. Theory Comput.* **2015**, *11*, 5665–5687.

(89) Joos, J. J.; Van der Heggen, D.; Martin, L. I. D. J.; Amidani, L.; Smet, P. F.; Barandiarán, Z.; Seijo, L. Broadband infrared LEDs based on europium-to-terbium charge transfer luminescence. *Nat. Comm.* **2020**, *11*, 3647.

(90) Visser, O.; Visscher, L.; Aerts, P. J. C.; Nieuwpoort, W. C. Molecular open shell configuration interaction calculations using the Dirac–Coulomb Hamiltonian: The f^6-manifold of an embedded EuO_9^{-6} cluster. *J. Chem. Phys.* **1992**, *96*, 2910–2919.

(91) Holzer, C.; Wernbacher, A. M.; Senekowitsch, J. M.; Gatterer, K.; Kelterer, A.-M. A Theoretical Study on Trivalent Europium: From the Free Ion to the Water Complex. *J A* **2014**, *118*, 11499–11511.

(92) Becke, A. D. Current density in exchange-correlation functionals: Application to atomic states. *J. Chem. Phys.* **2002**, *117*, 6935–6938.

(93) Komorovsky, S.; Cherry, P. J.; Repisky, M. Four-component relativistic time-dependent density-functional theory using a stable noncollinear DFT ansatz applicable to both closed- and open-shell systems. *J. Chem. Phys.* **2019**, *151*, 184111.

(94) Körbel, S.; Boulanger, P.; Duchemin, I.; Blase, X.; Marques, M. A. L.; Botti, S. Benchmark Many-Body *GW* and Bethe–Salpeter Calculations for Small Transition Metal Molecules. *J. Chem. Theory Comput.* **2014**, *10*, 3934–3943.

(95) Corzo, H. H.; Abou Taka, A.; Pribram-Jones, A.; Hratchian, H. P. Using projection operators with maximum overlap methods to simplify challenging self-consistent field optimization. *J. Comp. Chem.* **2022**, *43*, 382–390.

(96) Autschbach, J. Time-Dependent Density Functional Theory for Calculating Origin-Independent Optical Rotation and Rotatory Strength Tensors. *ChemPhysChem* **2011**, *12*, 3224–3235.

(97) Warnke, I.; Furche, F. Circular dichroism: electronic. *WIREs Comp. Mol. Sci.* **2012**, *2*, 150–166.

(98) Binnemans, K. Interpretation of europium(III) spectra. *Coord. Chem. Rev.* **2015**, *295*, 1–45.

(99) Zerulla, B.; Krstić, M.; Beutel, D.; Holzer, C.; Wöll, C.; Rockstuhl, C.; Fernandez-Corbaton, I. A Multi-Scale Approach for Modeling the Optical Response of Molecular Materials Inside Cavities. *Adv. Mater.* **2022**, *34*, 2200350.